Concepts of interactions in local probe microscopy

Kerssemakers, Jacob Willem Jozef

CHAPTER 2

INSTRUMENTATION:

THE CANTILEVER PROBE

CHAPTER 2. INSTRUMENTATION: THE CANTILEVER PROBE

2.1. INTRODUCTION

In 1982, Binnig and Rohrer presented the first results of a so-called scanning tunnelling microscope (STM).[1] It was a great achievement, by combining the technology of accurate positioning with a feedback system based on measurement of a tunnel current between a surface and a probe. The surprising performance of STM and its spin-off techniques are well established since then, and embrace the field of scanning probe microscopy (SPM).[2]

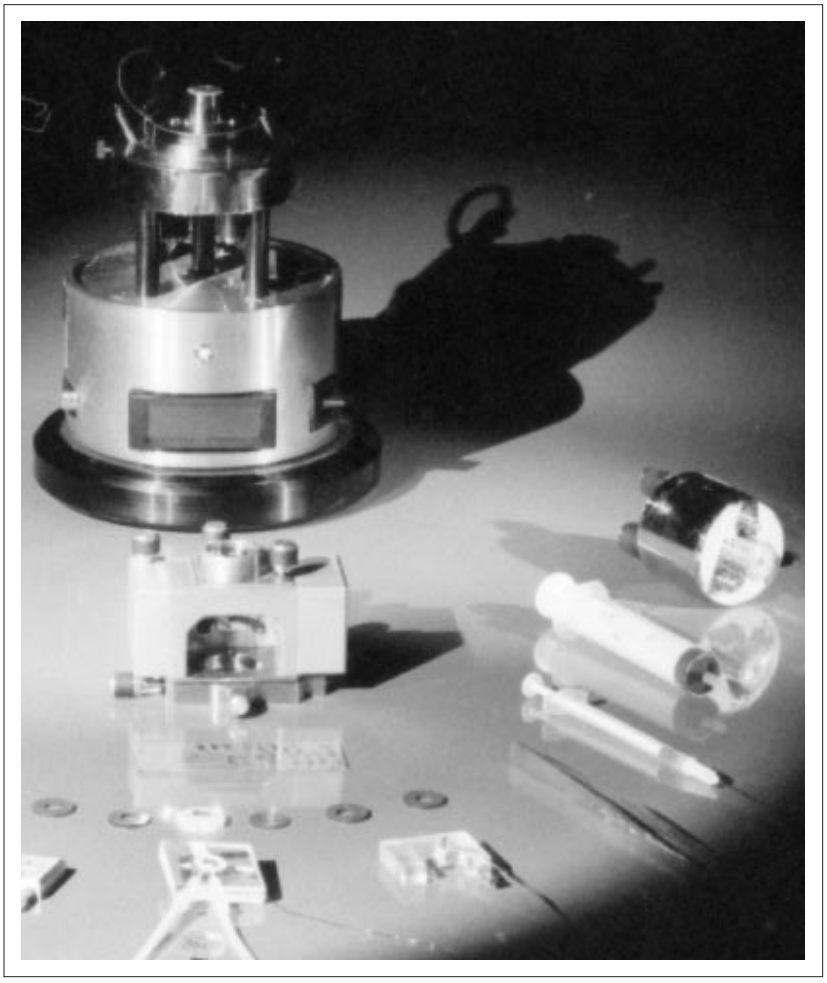

Figure 2:1. Decomposed Nanoscope II AFM. See also Figure 2:2.

Although the point resolution of STM is still not defeated by any other probe technique, a major disadvantage of STM is the demand for a (semi)conducting surface. In 1986, this problem was circumvented by inserting a conducting spring between an STM tip and a surface, thereby translating the interaction between surface and spring to movement of the latter, which subsequently was detected by a change in the tunnel current.[3] This technique denoted the introduction of Atomic Force Microscopy (AFM). A vast amount of detecting techniques have replaced the tunnel current detection system, but the essential part -namely the spring- survived. The principal part of any SPM is the probe. Commonly, a tip with nanometer sized radius of curvature is brought into interaction with a surface. The design of the probe determines the physical property which is measured. Because of the small dimensions of the probe end, the signal can be accurately located on a specific point of the surface, if the position of the probe is known. The latter is feasible by manipulating the probe or the surface relative to each other with some positioning device. Thus, an accurate positioning mechanism combined with a very local detection point forms the basis of any SPM. In a way it is remarkable that the SPM technology has more or less evolved back towards its origin: the field of scanning probe techniques started with STM, where the rather specific and exotic nature of tunnel current was employed. Contrary, in AFM the deformation of a probe is measured that is subjected to the cumulative interaction force of a surface or force field. The AFM approach can therefore be considered much more basic. This order of evolution stems mostly from instrumental considerations: although tunnelling as a physical property seems exotic, the demands on the tip itself are minor, since it only needs to be conducting. In contrast to this, measurement of a force necessarily means a translation of the force into a displacement by a mechanical spring device. Consequently, the performance of the Atomic force Microscope is principally governed by the properties of its probe spring, and the optimal dimensions of atomic force microprobes or cantilevers were only attainable incorporating IC-production technology. In this thesis the AFM plays the most prominent role and therefore Chapter 2 concentrates on the properties of the spring probe.

2.2. Optical lever AFM

2.2.1. Detection

Restricting ourselves to AFM, the most commonly used detection technique is the optical lever mechanism, introduced in 1988.[4,5] Here, a focused laser beam reflects from the end of a tilted cantilever. Attached to this cantilever is a tip. Each angular movement of this tip is amplified in the movement of the reflected laser beam. This beam tilt can easily and accurately be detected by a double- or quadruple split photodiode. This is a

simple yet accurate technique, working in any medium that allows a cantilever to move and a laser beam to pass through.

2.2.2. SCANNING AND POSITIONING

Like in most SPM's, scanning and positioning of tip and substrate are performed by piezoceramic actuators. Mostly a Z-direction is defined as being perpendicular to the average surface plane, the latter determining the XY-plane. At this point, we may make a distinction between imaging and point measuring, by considering the movements involved of the actuator. With imaging, the combination of coordinations X,Y,Z and the signal, or detected property, is used to make a more or less topographic plot of the surface. This can be a strict XY-plane, in fact a constant Z-measurement. However, usually it is of more practical value to present a constant-interaction plot, as this forms a more natural definition of the local surface. In this case, the Z-positioning is varied in such a way that during XY-movement, the force signal stays constant. This is simply implemented by comparing the detected signal to some reference value. The difference is used as an error signal in a feedback loop that regulates the Z-positioning.

A conceptually different approach is undertaken in point measuring. Here, the actuator is moved around a specific point in space. For instance, a distance dependence of the interaction can be measured by moving the actuator only in the Z-direction. Friction measurements on the other hand involve lateral (X-Y) movements. A study of the derivative of such a X- Y- or Z- dependent effect is commonly called spectroscopy. A problem involved with this approach is cross-talk between X-Y- and Z- planes, especially when the *local* surface deviates from the *global* surface orientation.

Recently, combinations of both approaches were introduced. For instance, in Tapping Mode[tm],[6,7,8] adhesion[9] and deformation[10,11] force microscopy techniques data is collected by repeated approaching and retracting of the tip on each point, creating a plot of the measured value. It is noted that for imaging, the demands on the origin of the detected interaction are somewhat less severe. The interaction mechanism is important to render image contrast, without a strict need to quantify the contrast. For instance, the signal contrast obtained when an AFM crosses an atomic step, consists of a complex mix of frictional and topographic properties of this step.[12,13,14] However the mere presence of a contrast is sufficient to investigate shape and properties of such a step, without the need to investigate the contrast mechanisms itself.

2.2.3. DESCRIPTION OF SET-UP

In this thesis, a Nanoscope II AFM was used,[15] as depicted in Figs.(2:1) and (2:2). In this instrument, the sample is moved while cantilever, laser and photodetector form a separate static unit, the head. By lowering this head the probe tip can be brought in to

contact with the sample which is mounted on the scanner unit. In this work, different scanners were used at different amplifications: A large scale scanner with a maximum range of ~9x9 μm^2 was used in the surface characterization in Chapter 3, while atomic friction experiments as described in Chapters 4 and 5 were performed with a more accurate 0.7 μm^2 scanner. Scanner and head are mounted on a housing, forming the AFM itself. A separate control unit is utilized for control of signals used in feedback, scanning and detection. Most of the tuning of system parameters during scanning is computerized.

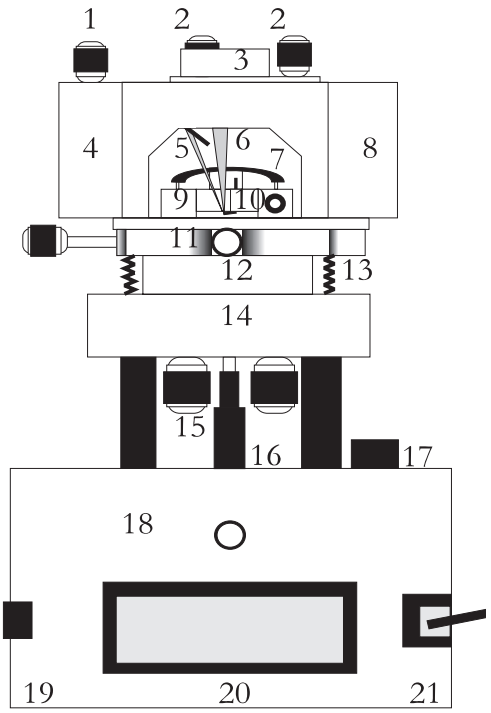

Figure 2:2. Front view, after Digital Instruments[15]

(1) Photodiode Y-adjustment
(2) Laser X-Y-adjustment
(3) Viewing window
(4) Photodiode housing
(5) Reflected laser beam and mirror
(6) Incident laser beam
(7) Holding arm
(8) Pre-amp housing
(9) Cantilever Mount
(10) Cantilever
(11) X-Y manual positioning stage
(12) Piezo tube scanner
(13) Head securing springs
(14) Scanner-support ring
(15) Coarse-approach screws
(16) Fine-approach stepper motor shaft
(17) Motor control switch
(18) Motor housing
(19) Controller connection socket
(20) Sum/Diff. detector signal display
(21) Display mode switch

The signal as acquired from the photodiode is stored as 400x400 data plots. This offers easy possibilities of processing data. All signals to and from the AFM, like piezo voltage and detector signal are transferred from the controller to the AFM as low voltage signals (-10V....+10V). For the sake of specific experiments, an extension unit was inserted in this connection which offers possibilities of manipulation of the piezo and loading behavior during one scan. This is an advantage when experimental drift becomes an important factor. Likewise, a special unit was designed to alter the scan pattern for the work described in Chapter 4. Valuable tools for actual experiments were an on-line storage oscilloscope and a speaker, both connected to the detector signal. The audio signal was used for tuning the atomic resolution imaging, since this is preferable when estimating the Fourier character and signal/noise ratio in periodic signals. A fluid cell supplied by Digital Instruments offers the possibility for scanning in liquid. In Chapters 4 and 5 this was implemented to circumvent capillary forces on the tip. These forces stem from a nanometer thick water layer on the substrate, always present in ambient air.[16,17] Another possibility of the fluid cell is immersing a substrate in an active medium. For instance, this can be etchant[18,19] as in Chapter 3 or electrolyte.[20,21]

2.3. THE CANTILEVER PROBE

The technical simplicity of the design of the optical deflection is a major reason for its popularity. Unfortunately, this simplicity does not extend to a theoretical description of the probing process. Here we will pay considerable attention to the central part of the AFM, namely the cantilever probe. For quantification, three aspects should be considered: Firstly, the mechanical properties of the cantilever. For most geometrical shapes, these are best described by a single spring constant or a set of spring constants. Secondly, the actual deformation of a cantilever, subjected to loading and frictional forces when pressed on a substrate. Thirdly, the detectability of this deformation by the photodetector during this.

2.3.1. MECHANICAL PROPERTIES

The commonly used cantilever design[15] consists of a Si_3N_4 V-shaped double beam with a pyramidal tip at the end, as shown in Fig.(2:3). To avoid unwanted beam-surface collisions, the cantilever is tilted with respect to the surface. In this configuration, the design is a compromise between different experimental demands on the probe. The V-shape was implemented to prevent sideways buckling, as the design was originally aimed at measuring topography. A coating with gold on the back side of the cantilever increases reflectivity, although there are some doubts about a better signal/noise ratio. [22] These cantilevers are fabricated, in batch, from one piece of silicon.

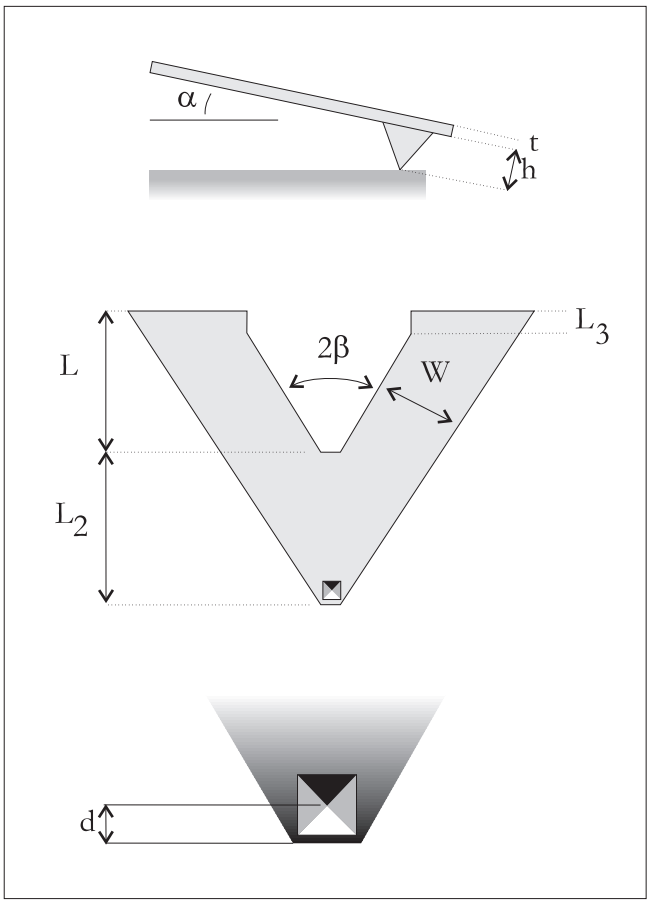

Figure 2:3. A typical cantilever with pyramidal tip

Some symbols used in the main text are denoted.

Table 2-I. Typical dimensions of V-shaped cantilevers;
partly after Butt et al.[23] See Fig. 2:3 for explanation of symbols.

Description	L μm	L_2 μm	L_3 μm	w μm	M,app.[23] kg
Short wide	58	55	7	22.5	$0.7.10^{-11}$
Long wide	111	82	10	37	$1.9.10^{-11}$
Short slender	69	43	9	14.5	$0.5.10^{-11}$
Long slender	152	39	10	21	$1.2.10^{-11}$

Common properties
material: Si_3N_4

d = 4-8 μm	E_{bulk} = 304 GPa
t = 0.5 μm	ν_{bulk} = 0.24
h = 3.5-4 μm	β = 28.5°

The surface is partly nitrided with the help of a mask, after which the silicon is etched away, leaving the produced upper layer of Si_3N_4 as the cantilever. Before nitriding, a tip is made in the silicon by preferential etching, resulting in a hollow pyramidal tip. V-shaped cantilevers are produced in four different types. Typical sizes and properties are given in Table 2-I (partly after Butt et al).[23] The variety in dimensions stems from different demands in different experimental circumstances. For instance, when imaging delicate live cells in liquid,[24] a large elevation range is to be combined with a low force, leading to long, slender cantilevers. The other extreme is more useful when imaging a hard, ionic surface. Then, a stiff cantilever provides a large force range. The V-shape is meant to prevent sideways buckling of the cantilever, which is considered a nuisance in topographic imaging. As will be shown, some different demands arise if friction forces are of interest.

Although the design of the cantilevers is more or less optimal in most circumstances, prediction of the mechanical properties suffers. The description of deformation of a cantilever under all possible moments and bending forces is essential for quantitative measurements. The forces are assumed to work on the tip point. The resistance force of the tip to a displacement in a certain direction can be associated with a stiffness. For small displacements the deformation of the cantilever is negligibly small, and a constant stiffness can be assumed.

However, unlike a simple one-dimensional spring, the stiffness of a cantilever is directionally dependent in three dimensions. For a given direction, the stiffness can be expressed as a combination of a small set of elastic constants. Apart from analytical approaches, a number of ways is available to determine one ore more of these elastic constants. Using finite elements (FE) methods, the predicted values of these constants bear the same accuracy as analytical results.[25,26.27] The largest errors in analytical as well as FE methods arise from the Young's modulus, Poisson's constant and the thickness of the Si_3N_4 cantilevers. Describing this as a smooth beam having perfect bulk properties is a rather severe assumption, causing deviations up to 50% from experimentally obtained values for the beam bending stiffness.[28]

Experimental methods avoid the major problem of using bulk material values for the rather thin, coated cantilevers.[28,29] At any rate, we still believe an analytical description may offer a better insight in the probing cantilever behavior. Moreover, experimental values for the beam stiffness can be used to predict other -e.g. torsional- elastic constants which are much harder to determine experimentally, from the analytical expressions. For a simple bar shape, we can easily discern three basic deformation modes, see Fig.(2:4), namely pure longitudinal bending, pure longitudinal torsion and pure transversal torsion. Because of the assumption of superposition, any arbitrary deformation can be split in these separate deformation modes. The two longitudinal

ones will result in a corresponding directional change of the laser beam, while the third causes a laser beam tilt perpendicular to this. With quadruple split photodetectors, this is utilized to obtain 'topographic' images from the longitudinal tilt, and 'friction' images from the lateral tilting of the reflected beam. However, we see that in doing this the longitudinal torsion component is neglected, which is not at all evident. We will use solely the longitudinal tilt components as in this thesis only a double split photodetector was employed.

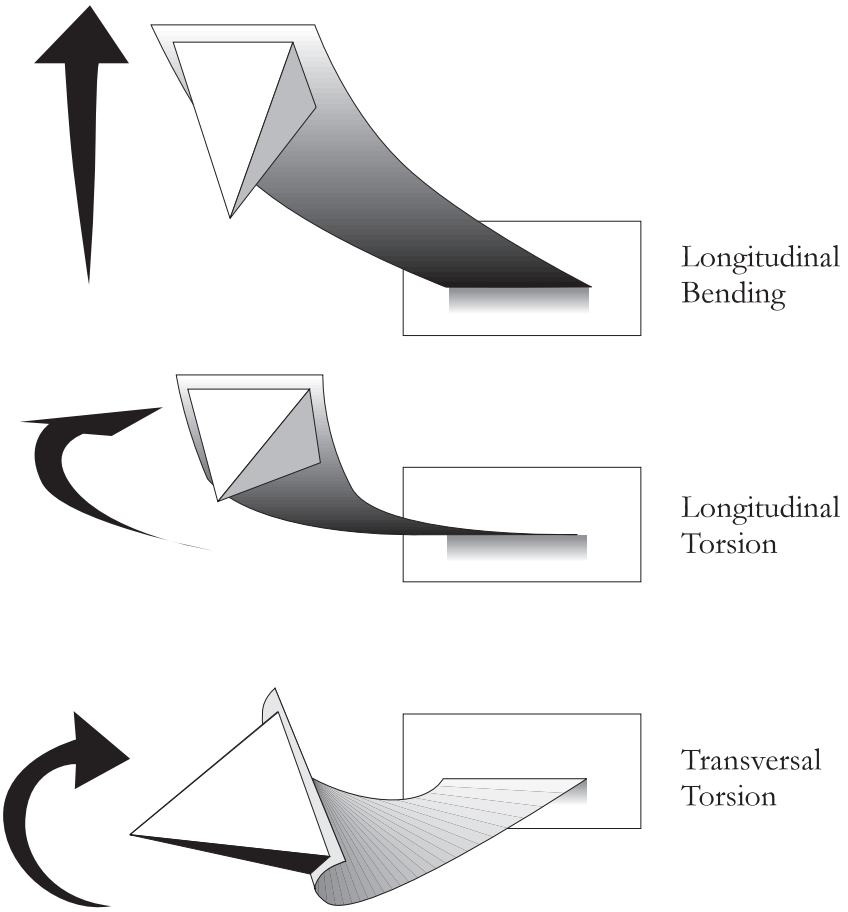

Figure 2:4. Three basic deformation types, shown for a bar shaped cantilever
Upper: normal bending, in which the cantilever beam length is a moment arm. Centre: longitudinal torsion, in which the bending direction is the same as in the upper case, but is caused by a force parallel to the cantilever beam, using the tip height as arm length. Lower: transversal torsion, caused by a tip moment similar to the centre case, but now perpendicular to the cantilever beam.

The cantilever is thought to be subjected to a load N perpendicular to the cantilever, a longitudinal bending moment M and a lateral bending moment T. All work at the tip end. In Chapter 5 the relation of N and M to surface load and friction will be worked out for a specific example. For now, we will only present the dependence of back end angles θ and ϕ and deflection Δ, see also Fig.(5A:1). These relations are

$$\begin{bmatrix} \phi \\ \theta \\ \Delta \end{bmatrix} \equiv \begin{bmatrix} C_\phi & 0 & 0 \\ 0 & C_\theta & C_{\theta z} \\ 0 & C_{z\theta} & C_z \end{bmatrix} \begin{bmatrix} T \\ M \\ N \end{bmatrix} \qquad (2:1)$$

with L the total cantilever length and where it turns out that $C_{\theta z} = C_{z\theta}$. These are zeroth-order solutions of a given deformation of the cantilever, which means that the different components can be superimposed on to each other. Because the displacements of AFM cantilevers in different directions seldom exceed 1% of the corresponding dimensions of the cantilever, this is a plausible assumption. Note that in the definition of compliances used here N was kept as a force, and not expressed as a moment. Because this N is approximately equal to the common loading force, this is a natural choice. In Table 2-II, the compliances associated with the three deformation modes are presented. Also presented are the corresponding angle changes at the normal detection point (directly above the tip) and the elastic curves of the cantilever. The latter two will become of importance if we discuss the reflection properties of the cantilever. For a V-shaped cantilever, double-bar expressions were initially used in de so-called parallel-beam approximation (PBA),[23] where the cantilever is approximated by a double bar-shape. Although this PBA yields compact solutions for the spring constant, the error due to approximation ranges from 16 to 25%, depending on the choice of the parameters. A comparative study by Sader[25] reduces this error to 2% by adding a triangular plate in the analysis. However, as soon as the cantilever is tilted and loaded, torsional and bending properties of the cantilever mix, and a more accurate description is preferable. Ogletree et al[31] presented an effective in-situ routine for any cantilever shape to calibrate the frictional force and the piezo at once, by utilizing a faceted $SrTiO_3$ substrate. The two well known

Table 2-II. Deflection and reflection properties of a bar shaped cantilever

force direction	compliance	back angle	elastic curve
load force N	$C_z = \frac{4L^3}{Ewt^3}$	$\theta_{max} = \frac{6NL^2}{Ewt^3}$	$\theta(x) = \frac{6F_x x}{Ewt^3}(2L - x)$
longitudinal moment M	$C_{\theta z} = \frac{6L^2}{Ewt^3}$	$\theta_{max} = \frac{12ML}{Ewt^3}$	$\theta(x) = \frac{3F_x hx}{Ewt^3}$
lateral moment T	$C_\phi = \frac{3L}{Gwt^3}$	$\phi_{max} = \frac{3TL}{Gwt^3}$	$\phi(x) = \frac{3F_y hx}{Gwt^3}$

orientations of the [103] and [101] facets on the surface allow to quantify the slope-up and the slope-down friction signal. Although this is a powerful method, it does not account for the exact position of the cantilever during scanning. This is important in modulation experiments, in which the force configuration is constantly changed.[32-34] Moreover, because such a method links the possible cantilever deformations, but does not provide an absolute value of stiffness, a complete view of the cantilever behavior still lacks. The rather complete description by Neumeister et al[26] only neglects the broadening of the cantilever base. The mechanical properties obtained are presented in a compact two-dimensional compliance matrix for longitudinal effects, and a simple expression for the sideways torsion ϕ. This representation is suitable for further analysis (see also Chapter 5). For an explanations of units see also Fig.(2:3). From the detailed expressions for the various compliances, we see the advantage of the compact matrix representation:

$$C_{\phi} = \frac{3}{Et^3}\left[\frac{(1+\nu)}{\tan\beta}\log(\frac{L_2}{d}+1) + \frac{2L(1+\nu)}{w}\left(\frac{\cos\beta}{2} - w\frac{6L\sin\beta\cos\beta + 3w(1+\upsilon)\cos^3\beta}{8L^2+3w^2(1+\nu)\cos\beta}\right)\right] \qquad (2:2a)$$

$$C_{\theta} = \frac{3}{Et^3}\left[\frac{2}{\tan\beta}\log(\frac{L_2}{d}+1) + \frac{2L(1+\upsilon)}{w}\left(\frac{1}{\cos\beta[2-(1-\nu)\cos^2\beta]}\right)\right] \qquad (2:2b)$$

$$C_{z} = \frac{3}{Et^3}\left[\frac{(L_2-d)^2 - d^2\left(1+2\log\left(\frac{L_2}{d}+1\right)\right)}{\tan\beta} + \frac{L^2}{w\cos^2\beta}\left(\frac{2L}{3\cos\beta} + L_2\cos\beta - r\sin\beta\right) + \frac{L(1+\upsilon)L_2}{w\cos\beta}\left(L_2 + \frac{r}{\tan\beta}\right)\right] \qquad (2:2c)$$

$$C_{\theta z} = \frac{3}{Et^3}\left[\frac{2}{\tan\beta}\left(L_2 - d\log\left(\frac{L_2}{d}+1\right)\right) + \frac{2L(1+\upsilon)}{w}\left(\frac{L/2+L_2}{\cos[2-(1-\upsilon)\cos^2\beta]}\right)\right] \qquad (2:2d)$$

$$C_{z\theta} = C_{\theta z} \qquad (2:2e)$$

From these expressions, we note that all compliances scale equally with the cantilever thickness t and the elastic modulus E of the material, Si_3N_4 . Therefore we assume that, although these parameters are rather hard to determine accurately, the relative magnitude of the compliances will not be affected. Then, if we compare for instance the cantilever deformations caused by load forces or frictional forces, the relative results

should be unaffected. This fact will be useful in a calibration routine presented in Chapter 5.

2.3.2. LOAD FORCE AND FRICTION

Once the mechanical properties of the isolated cantilever are obtained, the question is how these properties come into play in the actual set-up. While scanning along a substrate, the angular tilt of the tip can be due to purely topographic changes. However we should be aware of the fact that the angular change is caused by a moment and not by a force. It means that, although this moment can be caused by the combination of a perpendicular force and the cantilever length, and equally valid option would be a lateral force in combination with the non-zero tip height. Although this does not simplify analysis of the probe signal it offers a possibility to measure friction at a nanometer scale. The former implies that the same instrument can be used to measure topography, friction or a combination of both. Nevertheless, it is still possible to keep frictional and topographic studies separate, if one is careful in the experimental setup. We can associate friction and load roughly with two moment forces; a force F_x having the total tilted tip height $H=(h+t/2)$ as an arm, and a force F_z using the tilted beam length for this. Tilting can be incorporated by a simple rotation matrix between the force vector and the deformation vector of Eq.(2:1):

$$\begin{pmatrix} T \\ M \\ N \end{pmatrix} = [\mathrm{R}] \begin{pmatrix} HF_y \\ HF_x \\ F_z \end{pmatrix} \qquad (2:3)$$

A detailed analysis of this relation is presented in the Appendix of Chapter 5. Apart from forces on the cantilever and the corresponding angular change, we should now consider the displacements of the cantilever tip given a certain set of (ϕ,θ,Δ). This should be done carefully, as the tip displacement is essentially the only parameter which can be directly manipulated, by the piezo scanner. For instance, loading is done by forcing the tip plane straight upwards along the piezo Z-axis. If the tip would not move laterally, very strong buckling lateral forces would exist. Mostly, this doesn't happen, but the tip will inevitably start sliding during loading. In literature, vertical [10,33,35,36] and lateral [32,34] force modulation as well as plastic indentation have attracted considerable attention.

However, it is often overlooked that that instead of purely vertical indentation, the actual process consists of a mixture of indentation, friction and even ploughing. Performing, for instance , surface compliance experiments under these circumstances is rather dangerous. For this reason a detailed discussion on sliding is appropriate.

In first order, the displacements of an untilted cantilever (x,y,z) is simply identical to $(H\phi,H\theta,\Delta)$. Tilting just incorporates the rotation matrix [R] from Eq.(2:3), working on the

displacements. However, implementing second-order cross talk leads to the following expressions of the displacements:

$$\begin{pmatrix} x \\ y \\ z \end{pmatrix} = [R] \begin{pmatrix} H\theta + f(\Delta) \\ H\phi \\ \Delta + H\theta^2 + H\phi^2 \end{pmatrix} \tag{2:4}$$

Neglecting the second order terms in z seems justified, as in this work the lateral movements never exceed a few nanometers, contrary to loading deflections z of the cantilever which are two orders of magnitude higher. However, this means that the other way around the effect is strong: changes in load cause relatively strong lateral movements of the tip along the substrate surface. Given a curvature $\theta(\lambda)$ along a bar of length L of the cantilever, an expression for this extra shortening of the translation of the tip is

$$f(\Delta) = \int_L \tfrac{1}{2}\theta^2(l)_\Delta dl \tag{2:5}$$

In Fig.(2:5), a graph of this longitudinal movement of the tip of an untilted bar cantilever is shown. Combining this with tilt, and the much more complex behavior of the V-shaped cantilever, we see that, especially at small modulations, the relative sliding can be substantial. At large modulations, the governing term is the rotated deflection [R].Δ, which is positive for upward bending in a normal configuration. However, a finite friction coefficient leaves a torsional component M_μ , causing an opposite translation. As the frictional force causing this torsion depends on the load, a rather complex situation arises, in which all forces and deflections interfere.

Experimental evidence of tip sliding can clearly be seen in Fig.(2:5). Here we observe a surface wear track on a [100] vicinal plane of NaCl obtained by a piezo Z-modulation by a bar-shaped cantilever. The wear is mainly visible by the perturbed atomic steps, which make this wear track well visible, although the amount of transported material is extremely small. Material was transported in the direction of the increasing load, which is downward in this figure. A process like this should not be considered as an indentation experiment, independent of plasticity. The wear tracks deepen towards the high load side of the track, showing some removed material on the sides of the track. What should be kept in mind is that any change in load during scanning causes a mature sliding of the cantilever. Another consequence of cross talk is an erratic piezo feedback. The inverted friction in a backward and a forward longitudinal scan causes a change in the angle θ. The feedback loop causes the piezo to correct this by a Z-movement, which in turn causes lateral sliding. Because the change in friction is erratically balanced by a change in load, backward and forward scans will be performed under different loads.[37]

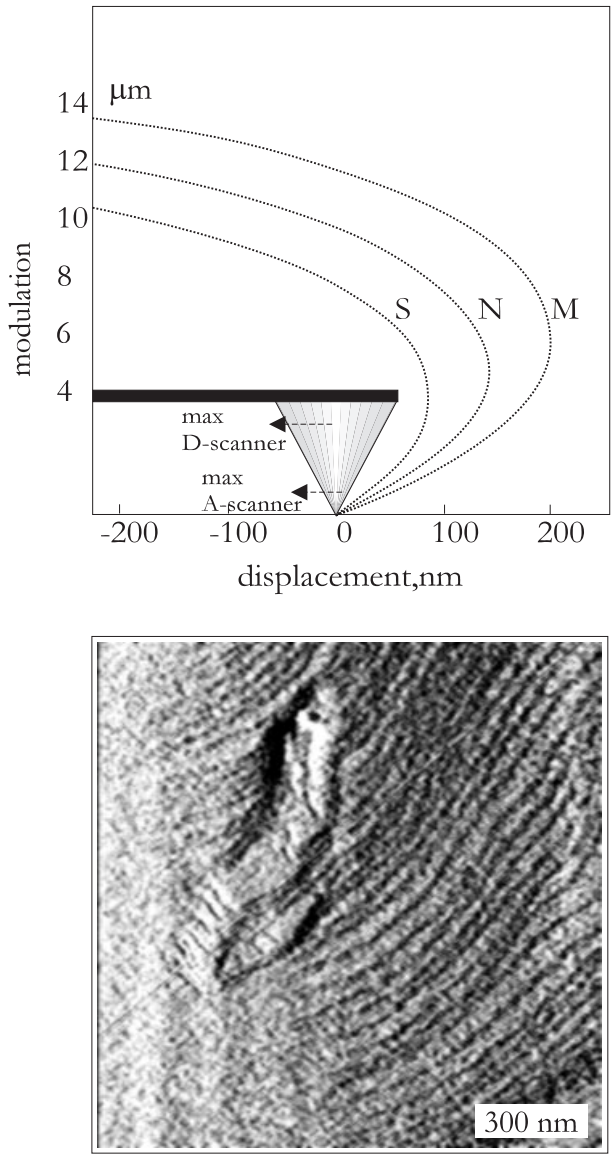

Figure 2:5. Crosstalk in cantilever movements

Upper: Due to the nonzero tip height, the tip of a cantilever will slide sideways under forces. Dashed lines: tip path followed when the tip of a bar shaped cantilever is subjected to a moment around the tip (M), a normal bending force (N) and for both when the cantilever beam is rigid (S). Arrows: modulation range of the two types of piezo scanners used. We see that especially in the case of small vertical modulations, the relative lateral movement can be substantial. Lower: Combined with loading forces, this leads to wear marks in the substrate. In this picture, we see atomic [100] steps disturbed by such a wear process with a 600 nm Z-modulation. From the morphology, we clearly see the occurrence of material transport towards the higher load (below) part of the scratch. Z-modulation should not be taken as a pure indentation process.

2.3.3. ELECTROSTATIC LOADING

Apart from the inevitable sliding, another disadvantage of loading by bending the cantilever with the piezo, is the small force range when weak cantilevers are used. This can be solved by using a more direct way of applying a force to the cantilever. It can be done magnetically[38] or by electrostatic loading. The latter approach was used in this work. For this technique, the cantilever is sputter coated on the lower side with a thin (~2-10 nm) conducting layer. Upon scanning, a relative voltage is applied between substrate and cantilever. The tip-end itself can easily be made non-conducting by a voltage pulse, i.e. blasting off the tip end coating: see (Fig.2:6). Although the loading works best with conducting substrates, some electrical force attraction is also experienced on insulating ones, probably due to polarization. A crude parallel plate capacitor model predicts a square dependence on voltage and distance from the surface.

This was tested by varying the tip height around fixed positions above the surface. It resulted in a parabolic surface plot reflecting the deflection as a function of voltage and height above the surface, shown in Fig.(2:6). Restricted by tip height and a breakdown voltage of order 10V, the estimated electrostatic force can be 10^2 N. For soft cantilevers this force is of the same order of magnitude as the force which can be applied using the 0.7 μm Z-range scanner. Another possibility of applying loads by electrostatic loading was utilized in Section 4.4.1. High (>10^5 Hz) frequency voltage oscillations cause a strong and well tunable decrease of 'stick/slip' friction at very specific frequencies, where presumably a higher-order cantilever resonance frequency is activated, causing high-frequency *lateral* movements of the tip.

2.3.4. REFLECTION PROPERTIES

Ideally, the laser beam should reflect in a point sized focal spot from the back of the cantilever, right above the tip. In practice, the laser spot is not doing this, but forms an intensity distribution over a curved reflected area. Within the scope of this work, we are not interested in the actual prediction of signal yield. However, the expressions presented before on the cantilever curvature (Table 2-II, elastic curves) can only be evaluated if the signal changes can be linked somehow to this deformation, otherwise corrections should be made.[39] The V-shaped cantilever expressions Eqs.(2:2a-e) are specifically evaluated for the angular change of the rigid tip and the reflecting area right on top of it. The most intense part of the laser spot should be right on this spot. Still there would be a contribution from the cantilever beams. Nevertheless, because the triangular end of a cantilever becomes increasingly less stiff towards the tip, we may expect that this tip area contributes most to the change in signal if the load on the cantilever is changed. This is displayed in Fig.(2:7), after Warmack et al.[37]

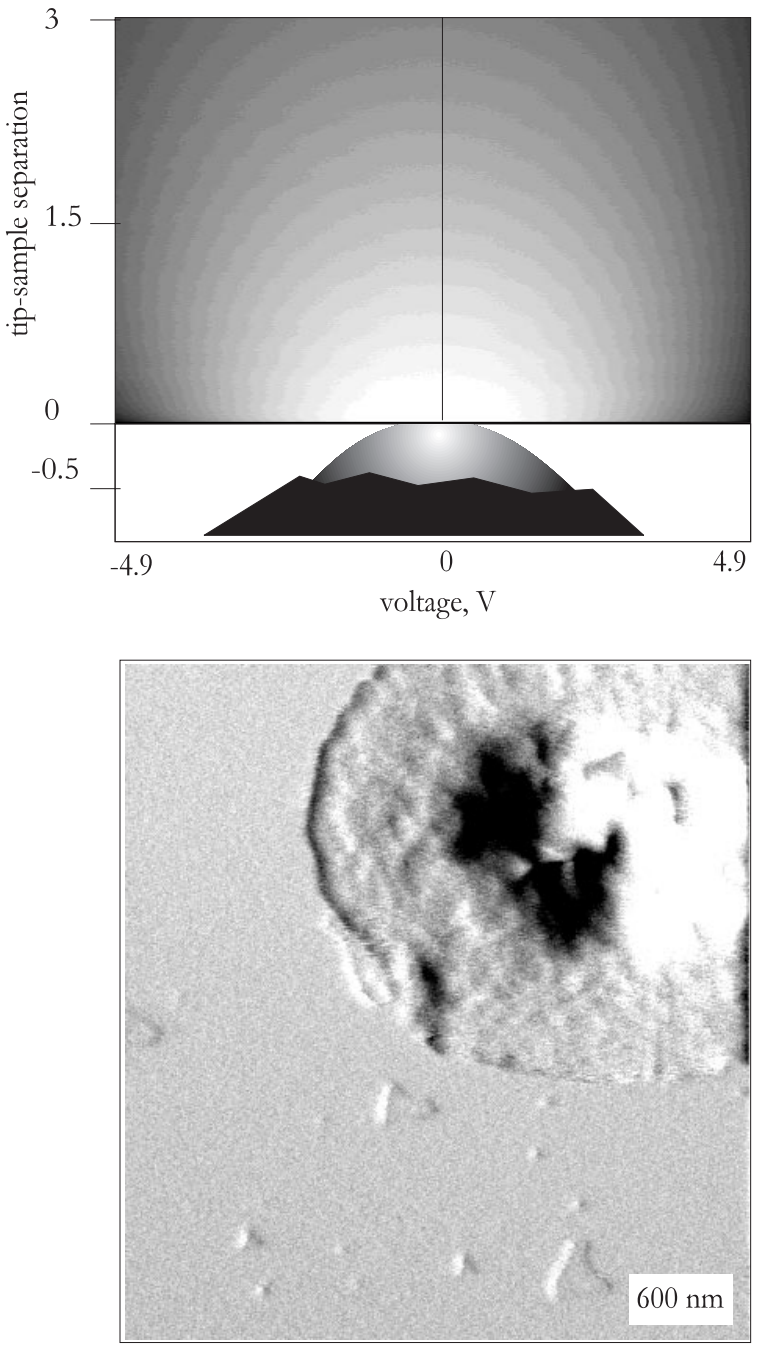

Figure 2:6. Electrostatic loading

Loading of an Au-coated cantilever by electrostatic forces decreases tip sliding effects. Upper: a two-dimensional measurement of cantilever deflection vs. applied tip-surface voltage, and tip end distance above the substrate. The closer to the surface, the more strongly the deflection response is, with downward=black. The electrostatic force stays finite at tip contact, because the tip end itself has been uncoated by a voltage pulse, leaving an Au grain on the surface. Such a deposited Au grain is shown in the lower image on an NbS_2 surface.

However, we may conclude from the above that tuning the laser spot position for maximum signal *yield* does result in the desired situation, because for maximum reflected intensity the spot will be more or less centered on the central part of the triangle end. Tuning the spot to maximum *sensitivity* is neither an optimal solution, because this optimum sensitivity is a trade-off between signal yield and amount of local bending. The optimal tip-centered configuration was accomplished in the following way.

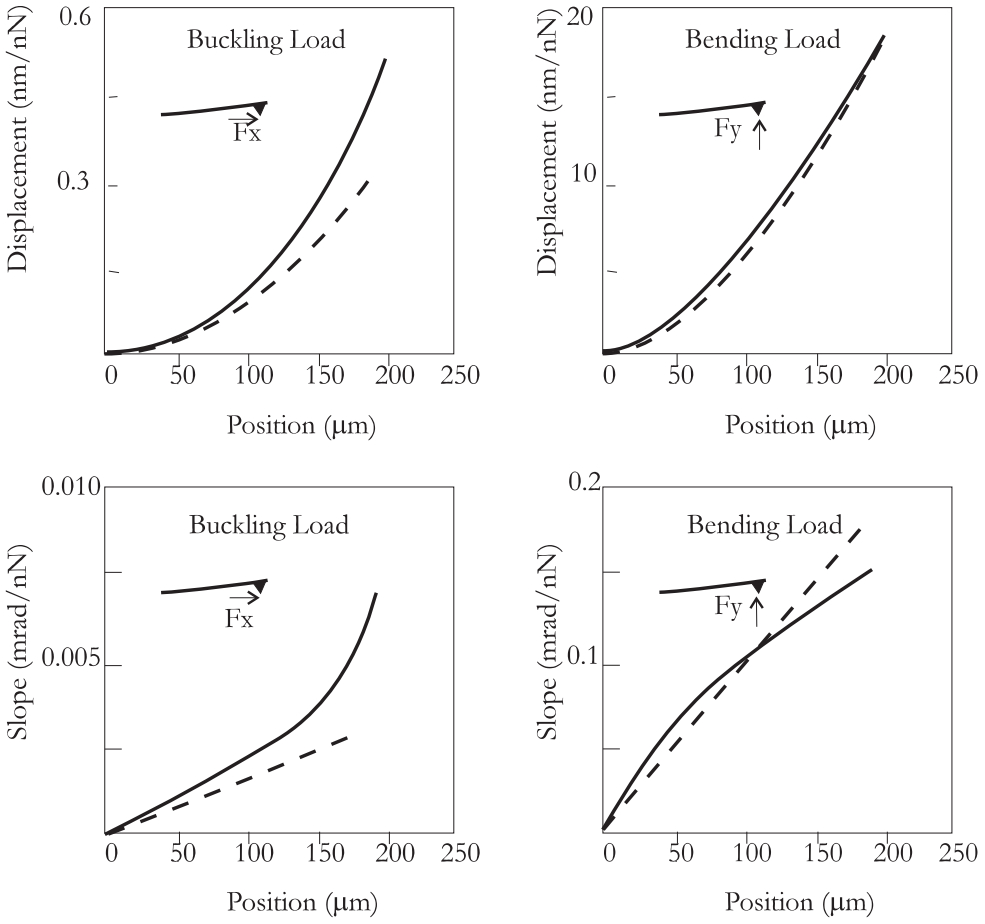

Figure 2:7, after Warmack et al [37]; Cantilever bending

Elastic curves (upper) and local slope (lower) under different load types. Dashed lines are for a bar shaped cantilever, while solid lines depict V-shaped cantilevers. The influence of friction relative to normal load is much larger in the case of a V-shape than it is for a bar shape.

First, a rough numerical estimation of the signal was done, centering a Gaussian profile on a point along the cantilever axis. Integrating the profile over the reflecting surface results in an intensity curve shown in Fig.(2:8).

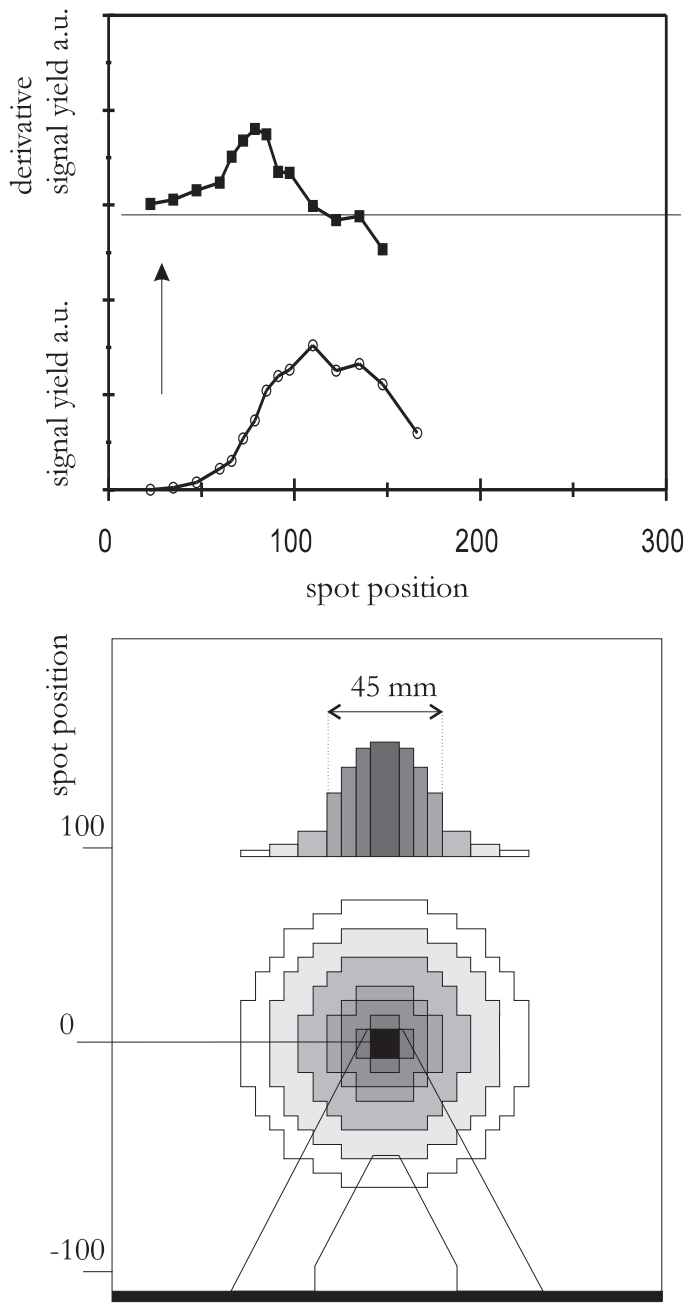

Figure 2:8. Tuning the laser spot

A rough numerical estimate of the signal-yield as a function of laser spot position on the back of a cantilever. The derivative of the intensity curve yields an estimate of the laser spot halfwidth.

In this approach, the spot profile is 'scanned' by the reflecting surface. As can be seen, at the edges of the cantilever the derivative of this intensity curve gives a measure for the spot size. Then, the same procedure performed on an actual cantilever results in Fig.(2:9). From the figure the width of the focused laser spot was estimated at three points: the cantilever holder edge, the edge of the inside opening of the cantilever, and the outer edge. Although all edges, due to their different shape, integrate the spot in a slightly different way, a common estimate for the spotsize was found of halfwidth radius ~22 μm. Then, centering this spotsize on the known tip point gives a measure of the *relative* yield at which the desired configuration is reached. We see this position should be expected around 70% of the maximum signal yield, while the point of maximum sensitivity is displaced some 10 μm from this, at 85 % of maximum signal yield. As the spot is smaller than the triangular plates for all types of cantilevers (see table 2-I), we assume these numbers to be valid for all of these cantilevers.

2.3.5. THE CANTILEVER TIP

The instrumental properties described in the above are aimed at measuring forces, centered on the tip, or more precisely, on the contact area between tip and surface. We may distinguish between a macroscopic and a microscopic tip shape. Macroscopically, the tip forms a near-perfect pyramid. The aspect ratio, or correspondingly the steepness of the side walls determine the height and scale of roughness which can be correctly monitored by the AFM tip. If certain characteristics of the surface exceed this tip sharpness, the images show an intricate mixture of tip and surface geometry. Very sharp surface features even tend to show a replica image of the tip pyramid itself, from which a clear example can be seen in Figure (2:10).

In this figure, an NaCl whisker of size 200x200x1300 nm was grown and imaged in a NaCl/ethanol/water solution. The beam-shaped whisker is clearly dilated with the pyramidal tip shape. However, in this work only rather smooth planar surfaces where investigated, where this problem does not arise. Microscopically, the end point of this pyramid is not atomically sharp, but forms a spheroid or parabolic shape. The corresponding tip radius of range 20-40 nm is of great importance in loading and friction experiments. This radius may vary considerably from cantilever to cantilever. Because of this a number of ways to determine tip shape or radius has been proposed. Scanning spike like features[40] or along atomically sharp edges of a $SrTiO_3$ substrate[41] yields two- and one-dimensional tip profiles, as in Fig.(2:10) after Carpick et al.[41] Indirect methods exist, based on continuum mechanical model fits to the loading curves. Rough estimates of tip size can be obtained from wear tracks, although in this case it is not as much the tip as well as a deformation zone that is measured (see also Section 5.2.3). Most results confirm the assumption that AFM tips are rather smooth paraboloids. The detailed atomic configuration should be comparable to the well known images of FIM

tips, yielding a nonperiodic surface. This non-periodicity will become of importance in Chapters 4 and 5, concerning stick/slip friction processes.

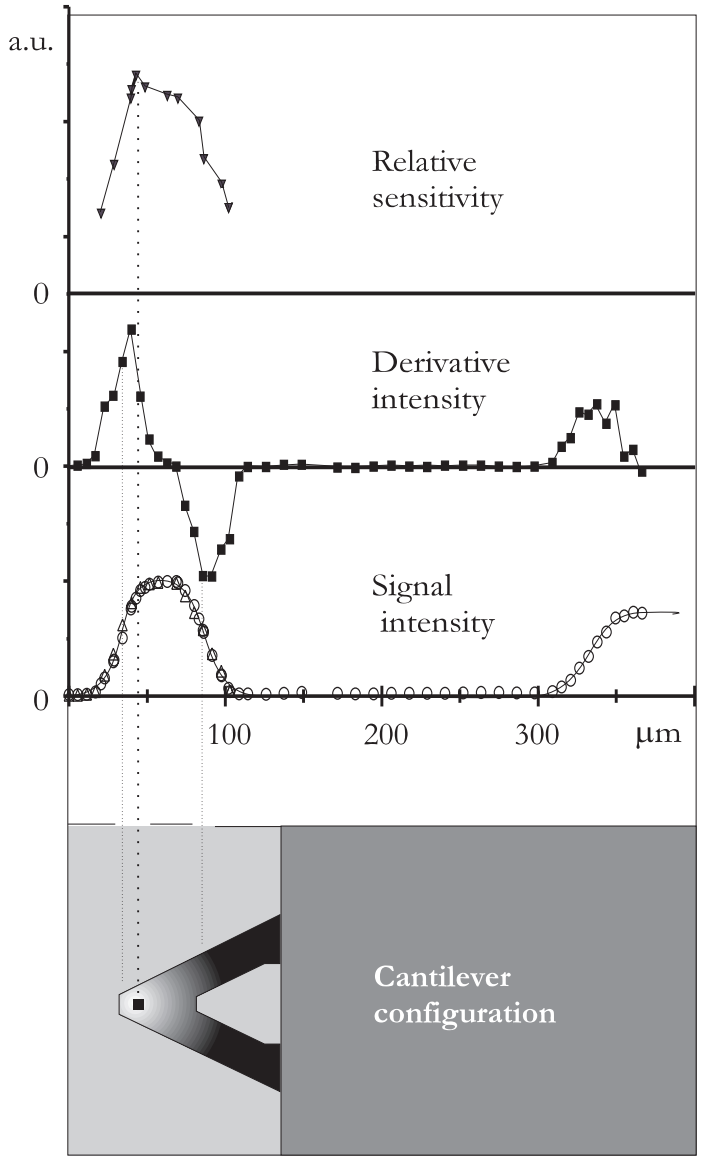

Figure 2:9. Tuning the laser spot

Using the result shown in Fig. 2:8, the intensity curve on an AFM cantilever was measured to obtain the approximate halfwidth of the laser spot. As can be expected (see main text) the desired tuning of the laser-spot right above the part of the cantilever that is most strongly curved, does not coincide with the highest intensity. In the upper curve this is confirmed: Z-modulation yields a signal response which is highest at about 70 % of the maximum signal yield attainable. Tuning the AFM to this point enables the use of bending analysis on actual cantilever configurations.

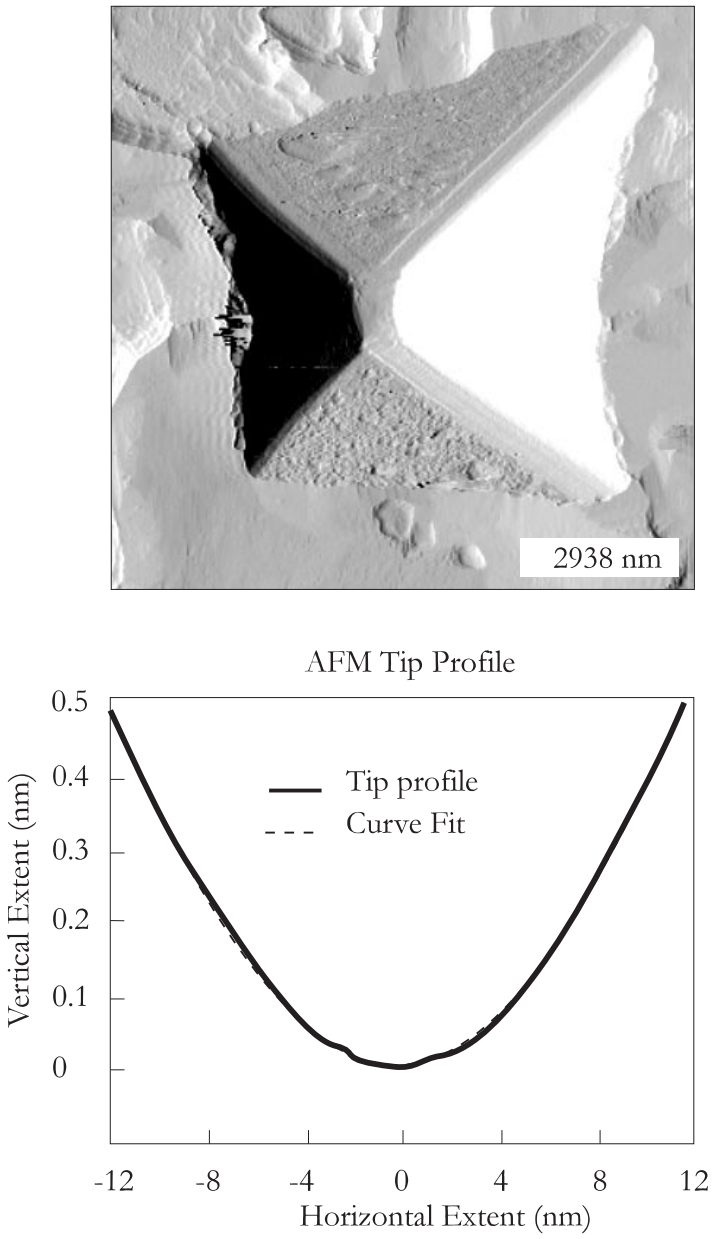

Figure 2:10. Tip shape

Upper: Tip artefacts. Slopes on a surface which exceed those of the pyramidal AFM tip, cannot be followed correctly by the tip. At spike like features, a replica picture of the tip emerges. An NaCl whisker of size 200x200x1300 nm was grown and imaged in an NaCl/ethanol/water solution. The beam-shaped whisker is clearly dilated with the pyramidal tip shape. Lower: after Carpick et al.[41] Atomic tip profile. By scanning a tip over the atomically sharp edges of a $SrTiO_3$ substrate, an accurate one-dimensional profile of the AFM tip can be obtained. The pyramidal tip is rounded at its very end, creating a parabolic curved tip with a radius of the order of 10^1 nm.

For now, in the case of smooth planes we may make a few remarks on resolution. Although point atomic resolution has been achieved with UHV AFM , in ambient air experiments the expected contact area, deduced from the above tip radius and typical capillary forces, exceeds atomic dimensions by a factor 10 or more. This lowers the resolution proportionally. The width as imaged of atomic steps reflects this, and imposes an upper limit on the density of such individual features. On smooth planes, the atomic corrugation detected is a collective friction effect and should not be confused with 'real' atomic resolution. However, the detection sensitivity of the probe itself was not an issue of importance in this work. A typical signal/noise ratio of a friction signal is 5:1.

In the following Chapters, we will make clear that the concept of 'resolution' depends on the type of experiments performed. It is not so much an intrinsic instrument property but depends on what type of interaction is primarily measured.

References

[1] G. Binnig, H. Rohrer, Ch. Gerber, E. Weibel, Phys. Rev. Lett. **49**, 57 (1982).

[2] S. N. Magonov, M_H. Whangbo, *Surface Analysis with STM and AFM*, VCH, 1996.

[3] G.Binnig, C.F. Quate, Ch.Gerber, Phys. Rev. Lett. **56**, 930 (1986).

[4] G. Meyer, N. M. Amer, Appl. Phys. Lett. **53**, 1045 (1988).

[5] S. Alexander, l. Hellemans, O. Marti, J. Schneir, V. Eilings, P.K.Hansma, M. Longmire, J. Gurley, J. Appl. Phys. **65**, 164 (1989).

[6] D. Sarid, T. G. Ruskell, R. K. Workman, D. Chen, J. Vac. Sci. Technol. B **14**, 864 (1996).

[7] J. Tamayo and R. Garcia, Langmuir **12**, 4430 (1996).

[8] A. Vinckier, F. Hennau, K. Kjoller, L. Hellemans, Rev. Sci. Instrum. **67** 387 (1996).

[9] V. N. Koinkar, B. Bhushan, J. Appl. Phys. **81**, 2472 (1997).

[10] M. R. Vanlandingham, S. H. McKnight, G.R.Palmese, R.F. Eduljee, J.W. Gillespie, JR. R.L. McCullough, JMS Lett. **16**, 117 (1997).

[11] R. Neumann, J. Ackermann, N. Angert, C. Trautmann, M. Dischner, T. Hagen, M. Sedlacek, Nucl. Instr. Meth. Phys. Res. B **116** 492 (1996).

[12] E. Meyer, R. Luthi, L. Howald, M. Bammerlin, M. Guggisberg, H.-J. Güntherodt, J.Vac. Sci. Technol. B **14,** 1285 (1996).

[13] E. Weilandt, A. Menck, O. Marti, Surf. Int. Anal. **23** 428 (1995).

[14] L. Howald, R. Lüthi, E. Meyer, G. Gerth, H. Haefke, R. Overney, H.-J. Güntherodt, J. Vac. Sci. Technol. B **12**, 2227 (1994).

[15] Digital Instruments, Santa Barbara, California USA.

[16] M.Bingelli, C. M. Mate, Appl. Phys. Lett. **65**, 415 (1994).

[17] T. Eastman and D.-M. Zhu, Langmuir **12**, 2859 (1996).

[18] D. W. Britt, V. Hlady, Langmuir **13**, 1873 (1997).

[19] P. A. Campbell, G. R. Ester, P. J. Halfpenny, J. Vac. Sci. Technol. B **14**, 1373 (1996).

[20] N. Ikemiya, K. Yamada, S. Hara, J. Vac. Sci. Technol. B **14**, 1369 (1996).

[21] P. W. Carter, A. C. Hillier, M. D. Ward, Mol. Cryst. Liq. Cryst. **242**, 53 (1994).

[22] M. Allegrini, C. Ascoli, P. Baschieri, F. Dinelli, C. Frediani, A. Lio, T. Mariani, Ultramicroscopy **42-44**, 371 (1992).

[23] H.-J. Butt, P.Siedle, K. Seifert, K. Fendler, T. Seeger, E. Bamberg, A. L. Weisenhorn, K. Goldie, A.Engel, J. Micr. **169**, 75 (1993).

[24] A. Ciancio, Eur. Micr. Anal. July, 5 (1994).

[25] J. E. Sader, Rev. Sci. Instr. **66**, 4583 (1995).

[26] J. M. Neumeister, W.A. Ducker, Rev. Sci. Instrum. **65**, 2527 (1994).

[27] M. Labardi, M. Allegrini, M. Salerno, C. Frediani, C. Ascoli, Appl. Phys. A **59**, 3 (1994).

[28] T. J. Senden and W. A. Ducker, Langmuir **10**, 1003 (1994).

[29] J. P. cleveland, S. Manne, D. Bocek, P. K. Hansma, Rev. Sci. Instr. **64**, 403 (1993).

[30] J. E. Sader, Rev. Sci. Instrum. **66**, 4583 (1995).

[31] D. F. Ogletree, R. W. Carpick, M. Salmeron, Rev. Sci. Instrum. **67**, 3298 (1996).
[32] R. W. Carpick, D.F. Ogletree, M. Salmeron, Appl. Phys. Lett. **70**, 1548 (1997).
[33] N. A. Burnham, G. Gremaud, A.J. Kulik, P.-J. Gallo, F.Oulevey, J. Vac. Sci. Technol. B **14**, 1308 (1996).
[34] T. Göddhenrich, S. Müller, C. Heiden, Rev. Sci. Instrum. **65**, 2870 (1994).
[35] A. B. Mann, J.B. Pethica, Appl. Phys. Lett. **69**, 907 (1996).
[36,] M. A. Unger, S. D. O'Connor, J. D. Baldeschwieler, J. Vac. Sci. Technol. B **14**, 1302 (1996).
[37] R. J. Warmack, X.-Y. Zheng, T. Thundat, D. P. Allison, Rev. Sci. Instrum. **65**, 394 (1994).
[38] S. P. Jarvis, A. Oral, T. P. Weihs, J. B. Pethica, Rev. Sci. Instrum. **64**, 3515 (1993).
[39] U. D. Schwarz, P. Köster, R. Wiesendanger, Rev. Sci. Instrum. **67**, 2560 (1996).
[40] L. Montellius, J.O. Tegenfeldt, P. van Heeren, J. Vac. Sci. Technol. B **12**, 2222 (1994).
[41] R.W. Carpick, N. Agrait, D. F. Ogletree, M. Salmeron, J. Vac. Sci. Technol. B **14**, 1289 (1996).